Composite Structures 195 (2018) 45–59

Contents lists available at ScienceDirect

Composite Structures

journal homepage: www.elsevier.com/locate/compstruct

Dynamic compressive response of additively manufactured AlSi10Mg alloy hierarchical honeycomb structures

Yuwu Zhang[a], Tao Liu[a,*], Huan Ren[a], Ian Maskery[b], Ian Ashcroft[b]

[a] Centre for Structural Engineering and Informatics, Faculty of Engineering, University of Nottingham, University Park, Nottingham NG7 2RD, UK
[b] Centre for Additive Manufacturing, Faculty of Engineering, University of Nottingham, University Park, Nottingham NG7 2RD, UK

ARTICLE INFO

Keywords:
Honeycomb
Mechanical properties
Impact behaviour
Finite element analysis (FEA)
Additive manufacturing

ABSTRACT

Periodic honeycombs have been used for their high strength, low weight and multifunctionality. The quasi-static and dynamic compressive responses of three types of additively manufactured AlSi10Mg honeycomb structures, specifically a single-scale honeycomb and two hierarchical honeycombs with two and three levels of hierarchy, respectively, have been investigated using experimental measurement and finite element (FE) simulations. The validated FE simulation has been employed to investigate the effects of relative density of the honeycombs and the key experimental parameters. The following failure modes of the three types of honeycombs have been observed both under quasi-static and dynamic compression: (1) the single-scale honeycomb experienced a transition of failure mechanism from local plastic buckling of walls to local damage of the parent material without buckling with the increase of the relative density of the honeycomb; (2) the hierarchical honeycombs all failed with parent material damage without buckling at different relative densities. For both quasi-static and dynamic compression, the hierarchical honeycombs offer higher peak nominal wall stresses compared to the single-scale honeycomb at low relative density of $\bar{\rho} = 0.19$; the difference is diminished as relative density increases, i.e. the three types of honeycombs can achieve similar peak wall stresses when $\bar{\rho} \geqslant 0.26$. Numerical results have suggested the hierarchical honeycombs can offer better energy absorption capacity than the single-scale honeycomb. The two-scale and three-scale hierarchical honeycombs achieved similar peak nominal wall stresses for both quasi-static and dynamic compression, which may suggest that the structural performance under out-of-plane compression is not sensitive to the hierarchical architecture. This work indicates that the structural advantage of hierarchical honeycombs can be utilised to develop high performance lightweight structural components.

1. Introduction

Periodic honeycombs have been used to create lightweight structures with high stiffness/strength-to-density ratios [1]. Wicks and Hutchinson [2] investigated the structural efficiency of sandwich plates with truss lattice cores and honeycomb cores under 3-point bending. They demonstrated that the minimum weight of a hexagonal honeycomb core sandwich plate was less than those of truss lattice core sandwich plates as well as a monolithic plate. Liu et al. [3] investigated the multifunctional performance of honeycomb core sandwich cylinders under simultaneous internal pressure and active cooling. They demonstrated that the sandwich constructions were more weight efficient than a monolithic structure while providing the additional benefit of an active cooling function. Hutchinson and Xue [4] demonstrated that a well-designed square honeycomb core sandwich plate could sustain significantly larger blast impulses than a solid plate of the same mass.

The in-plane topology of honeycombs can be designed to have either a 'bending-dominated' deformation mode under macroscopic in-plane stresses, such as hexagonal and square honeycombs, or a 'stretching-dominated' deformation mode, such as triangular honeycombs. The in-plane stiffness and strength of hexagonal honeycombs scale with $\bar{\rho}^3$ and $\bar{\rho}^2$ [4,5], respectively, with $\bar{\rho}$ being the relative density of the honeycombs. For stretching-dominated honeycombs, in-plane stiffness and strength scale linearly with $\bar{\rho}$ [4,5]. Though stretching-dominated structures possess greater in-plane elastic modulus and yield strength than bending-dominated structures, they suffer the disadvantage of post-yield softening behaviour owing to structural buckling [6].

Periodic, hierarchical honeycombs have recently emerged by combining in-plane geometrical elements at different length scales, see [4,7,8] and Fig. 1. Oftadeh et al. [9] investigated the in-plane

* Corresponding author.
E-mail address: Tao.Liu@nottingham.ac.uk (T. Liu).

https://doi.org/10.1016/j.compstruct.2018.04.021
Received 18 August 2017; Received in revised form 31 January 2018; Accepted 2 April 2018
Available online 03 April 2018

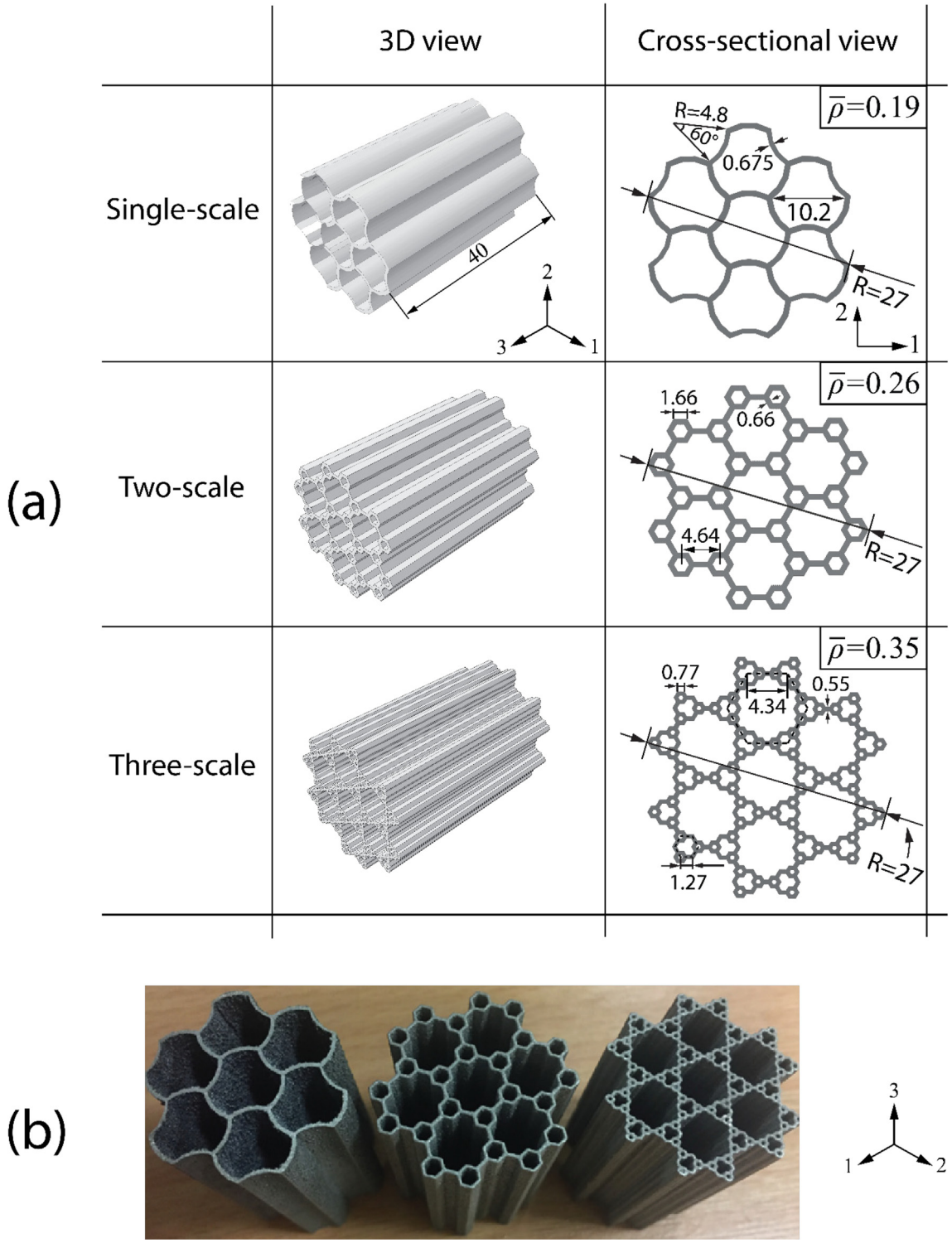

Fig. 1. The (a) sketch and (b) photograph of the Selective Laser Melting (SLM) manufactured single-scale, two-scale and three-scale honeycombs. All dimensions are in mm.

mechanical behaviour of hierarchical honeycombs with various hierarchical levels. They found that increasing the hierarchical level could significantly increase the in-plane effective elastic modulus of the honeycomb. For example, the two-scale and three-scale hierarchical honeycombs were 2.0 and 3.5 times, respectively, stiffer than the standard hexagonal honeycomb with identical relative density [8]. Hierarchical honeycombs also have higher in-plane collapse strength than standard hexagonal honeycombs with identical relative density [7]. With increasing hierarchical level, there is a transition of in-plane failure mode from elastic buckling to plastic buckling [10]. However, increases in the in-plane collapse strength were only seen to be significant for the first, second and third levels of hierarchy; higher hierarchical level did not significantly increase performance [7].

The out-of-plane stiffness and strength of periodic honeycombs are much greater than those along the in-plane directions [4,7,11]. For example, the out-of-plane compressive strength of aluminium

hexagonal honeycomb is 2 times greater than the in-plane compressive strength [11]. Extensive studies on the out-of-plane compressive behaviour of regular honeycombs have been reported in the literature [12–16]. As reported by Radford et al. [12], stainless-steel square honeycombs with relative density $\bar{\rho} = 0.1$ failed with torsional plastic buckling under quasi-static out-of-plane compression. Using Kolsky pressure bar testing with a striker velocity up to 300 ms^{-1}, they found that the dynamic compressive response was governed by three distinct mechanisms: material rate sensitivity, inertial stabilization of the webs against buckling, and plastic wave propagation [12,13]. Tao et al. [14] investigated the out-of-plane dynamic behaviour of hexagonal thin-wall aluminium honeycombs using a Split Hopkinson Pressure Bar (SHPB) at strain rates up to 1350 s^{-1}. They found that the failure mode was plastic buckling with significant strain rate enhancement, and that the buckling location and sequence depended on the strain rate and size of honeycomb cells.

Understanding of the out-of-plane compressive behaviour of metallic hierarchical honeycombs, however, is not well established. Numerical investigation has suggested that hierarchical honeycombs may possess improved energy absorption capability and greater resistance to out-of-plane crushing compared to regular honeycombs [16]. However, the manufacturing issue of hierarchical honeycombs was not considered in the numerical investigation. Conventional manufacturing approaches may encounter difficulty in manufacturing metallic hierarchical honeycombs owing to their complex 3D geometries. Selective Laser Melting (SLM), a layer-by-layer additive manufacturing technique, can be employed to overcome this difficulty. It is a cost-effective process to manufacture structural components whose geometrical complexity is prohibitive for conventional manufacturing technologies [17,18]. In this paper, we aim to gain insight into the behaviour of SLM manufactured metallic hierarchical honeycombs under static and high strain rate, out-of-plane compression, through both experimental measurement and numerical simulations. The outcome will provide the basis for the development of high performance, SLM manufactured, hierarchical honeycomb core sandwich structures. The outline of the paper is as follows. The materials and manufacturing methodology for honeycombs are presented in Section 2. In Section 3, the quasi-static and dynamic experimental protocols are explained. The finite element simulation is described in Section 4 and in Section 5, the experimental and simulation results are discussed.

2. Material and manufacturing

2.1. The honeycomb specimens

Three types of cylindrical honeycomb specimens were manufactured using Selective Laser Melting (SLM): single-scale, two-scale and three-scale, schematics and photographs of the honeycombs are shown in Fig. 1(a) and (b), respectively. They were made from AlSi10Mg alloy. Throughout this paper, the global coordinates are defined with the 3-axis aligned with the out-of-plane direction of the honeycombs, and the 1-axis and 2-axis representing the in-plane directions of the honeycombs. Each specimen has an out-of-plane (3-axis direction) thickness of $H = 40$ mm and an in-plane (1–2 plane) maximum diameter of $D = 27$ mm. The single-scale honeycomb specimens consist of 7 identical curved hexagonal unit cells with average wall thickness 0.675 mm, radius of each curved side 4.8 mm and central angle 60°. The design is motivated by Bauer et al. [19], which demonstrates that it can offer higher specific compressive strength than typical, straight-walled honeycomb geometry.

Hierarchical honeycombs have been reported to have good in-plane mechanical behaviour, as reviewed in Section 1. To examine their out-of-plane compressive behaviour, the two-scale and three-scale honeycombs were designed with in-plane hierarchical structures, i.e. combination of hexagons at two length scales for the two-scale honeycomb, and at three length scales for the three-scale honeycomb. The two-scale honeycomb consists of 7 large hexagons, each containing 6 smaller hexagons. The average wall thickness of the specimens is 0.66 mm, and the lengths of each side of the larger and smaller hexagons are 4.64 mm and 1.66 mm, respectively. The three-scale honeycomb consists of 7 large hexagons, each containing 6 medium-sized hexagons, which in turn contains 3 small hexagons. The average wall thickness of the sample is 0.55 mm, and the lengths of each side of the largest, medium-sized and smallest hexagons are 4.34 mm, 1.27 mm and 0.77 mm, respectively. The geometrical parameters of these honeycombs are mainly determined by the limitation of the manufacturing facility. The relative density $\bar{\rho}$ of the honeycombs is defined as $\bar{\rho} = \rho/\rho_0$, where ρ and ρ_0 denote the densities of the honeycombs and the AlSi10Mg alloy parent material, respectively. The measured relative densities of the honeycombs were 0.19, 0.26 and 0.35 for single-scale, two-scale and three-scale honeycombs, respectively.

2.2. Manufacturing

A Renishaw AM250 SLM machine was used to manufacture the specimens, comprised of dog-bone shaped coupons and the honeycombs. The principal chemical composition of the constituent material of AlSi10Mg powder contains Al 88.9 wt%, Si 10.7 wt%, Mg 0.5 wt%, and the powder particle size ranges from 15 μm to 110 μm. The optimised manufacturing process described in [20,21] was adopted to produce parent material with minimal porosity. The Renishaw AM250 SLM machine was equipped with an Yb fibre laser of power 200 W and wavelength 1070 nm. The laser scan strategy was chessboard and a scan speed of approximately 570 mm/s was achieved by employing 80 μm point distance and 140 μs exposure time. The hatch spacing was 130 μm. During processing, the AlSi10Mg powder was deposited in 25 μm layers with the temperature of the build platform being held at 180 °C. The specimens were manufactured under argon atmosphere with an oxygen content less than 0.09%. Both the honeycombs and dog-bone shaped coupons were manufactured with their 3-axis along the SLM build direction. The mechanical behaviour of the AlSi10Mg alloy parent material was characterised via coupon tensile tests, as described next.

2.3. Quasi-static tensile coupon tests of the parent material

In order to characterise the mechanical behaviour of the AlSi10Mg alloy parent material, quasi-static uniaxial tensile tests were conducted using dog-bone shaped coupons and the method described by ASTM standard E8/E8M [22]. The SLM manufactured test coupons had dimensions of gauge length 45 mm and diameter 9 mm, as schematically shown in the insert of Fig. 2. The coupons were manufactured with the longitudinal direction of the coupons aligned with either the 3-axis or 1-axis (2-axis). The uniaxial tensile stress was measured using an Instron 5581 screw-driven testing machine at a constant extension rate of 0.5 mm/min. A single Stingray F146B Firewire Camera video gauge was used to measure the corresponding nominal strain. Fig. 2 shows the measured nominal stress–strain relationship using the coupons with longitudinal direction aligned with either 3-axis or 1-axis (which was shown experimentally to be nearly identical to the 2-axis). For both alignments, the coupons exhibit the same linear elastic behaviour of average Young's modulus $E = 69.3$ GPa and yield strength $\sigma_y^0 = 160$ MPa. However, the coupon aligned with the 1-axis (or 2-axis) has higher tensile strength and greater ductility than that aligned with the 3-axis. Similar anisotropy has been seen in previous work and ascribed to microstructural anisotropy stemming from the asymmetric heat flux during laser irradiation and cooling and from the preference for flaws to align in this direction [23]. The microstructures of the SLM manufactured AlSi10Mg alloy using the same materials and process as used in this study have been previously reported by Aboulkhair et al. [24].

The experimental results shown in Fig. 2 are comparable to those of

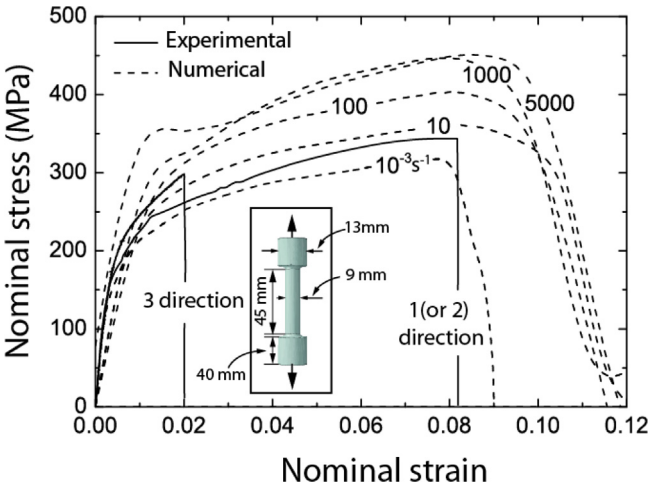

Fig. 2. The uniaxial tensile stress - strain relation of AlSi10Mg alloy at selected strain rates. The insert shows the geometry of the dog-bone coupon employed in the quasi-static test.

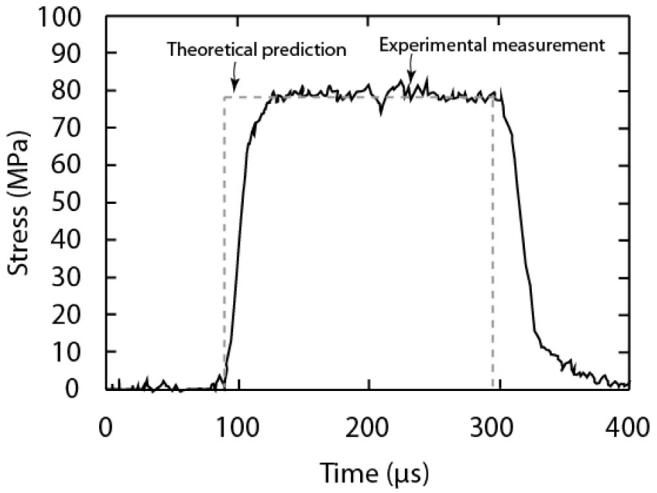

Fig. 4. Time history of stress measured by the Kolsky pressure bar setup during a calibration test.

the SLM manufactured AlSi10Mg alloy reported by Kempen et al. [18]. The tensile behaviour in the 1-axis or 2-axis direction was nearly identical to that of the cast AlSi10Mg alloy as reported by Manfredi et al. [25] and Joseph et al. [26]. In Section 4, the uniaxial tensile test results are used as the input of the constitutive model employed in the finite element simulations.

Table 1
Material properties for the SLM manufactured AlSi10Mg alloy.

Property	E	ν	ρ_0	C	$\dot{\varepsilon}_o$	ε_f	ε_c
Value	69.3 GPa	0.3	2.67 g·cm^{-3}	0.02	10^{-3} s^{-1}	0.08	0.0075

3. Experimental protocols for honeycombs under compression

3.1. Quasi-static compression testing

Quasi-static out-of-plane compression tests were conducted using an Instron® 5581 screw-driven testing machine with a constant displacement rate of 2 mm/min in the out-of-plane direction (3-direction in Fig. 1). The compressive force F and the vertical displacement δ of the crosshead were both directly measured from the testing machine. The nominal compressive strain and stress of the honeycomb specimens were calculated as $\varepsilon = \delta/H$ and $\sigma = F/A$, respectively, where H is the original height of the honeycomb specimens and A the original cross-sectional area of the honeycomb specimens, $A = \pi D^2/4$. The averaged wall stress $\overline{\sigma}$ of the honeycomb specimens can be related to nominal compressive stress σ and relative density $\overline{\rho}$ via $\overline{\sigma} = \sigma/\overline{\rho}$. A Phantom Mercury HS V12.1 high-speed camera was used to record the compressive deformation histories of the honeycombs.

3.2. Dynamic compressive testing

The dynamic out-of-plane compressive response of the SLM manufactured honeycombs was measured via a set of direct impact tests with a strain-gauged Kolsky pressure bar setup [12,27,28], as shown in Fig. 3. Two types of impact test were employed: back face and front face impact. For back face impact, a striker was accelerated through the gun

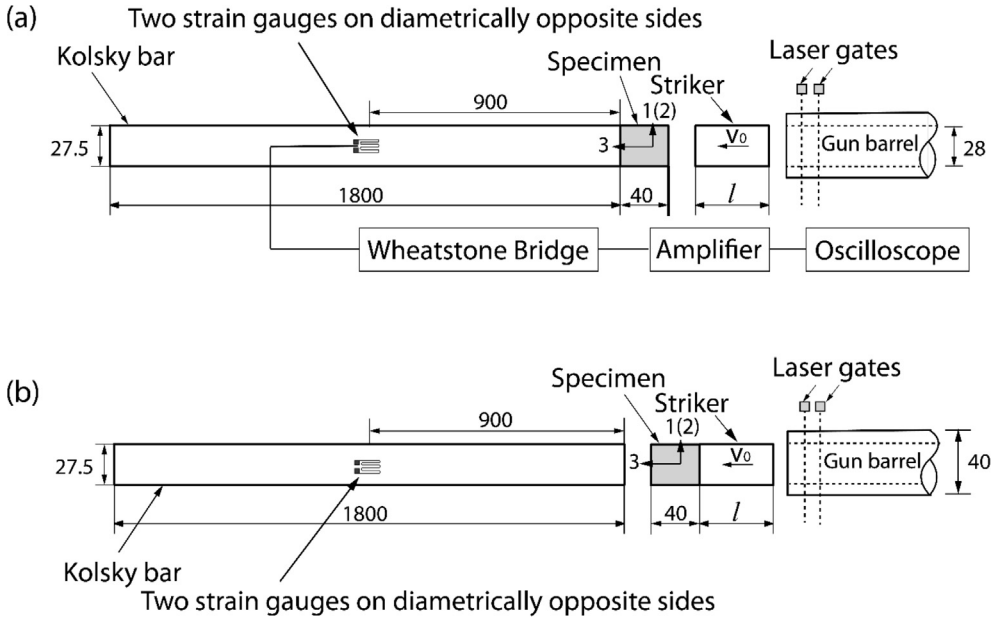

Fig. 3. Sketches of Kolsky bar setup employed in the experiment. (a) back face and (b) front face impact. All dimensions are in mm.

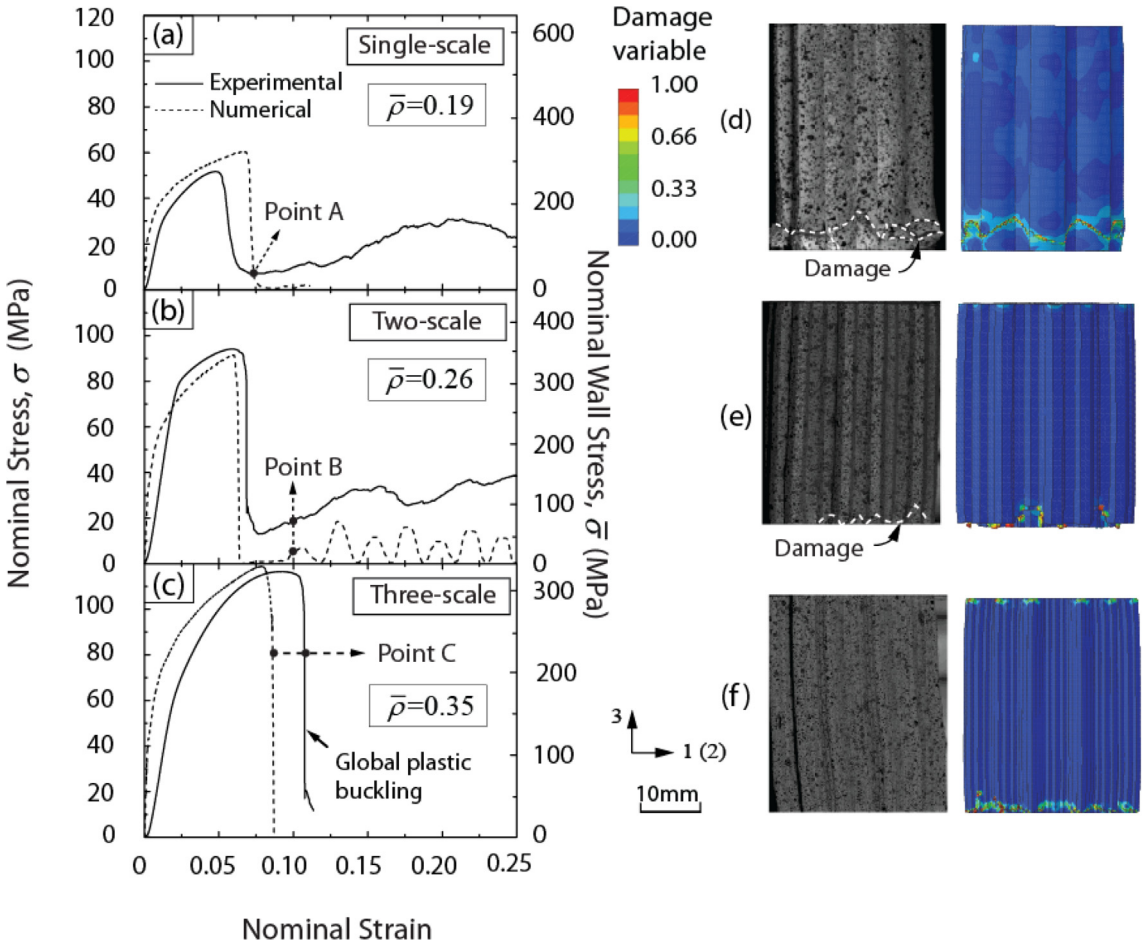

Fig. 5. Honeycombs under quasi-static compression. (a)-(c) Compressive stress–strain relations of the three types of honeycombs, and (d)–(f) experimentally measured (left) and FE predicted (right) damage mechanisms at Point A in (a), Point B in (b), and Point C in (c), respectively. The white dash lines in (e) and (f) show the damage locations of the single-scale and two-scale honeycomb, respectively.

barrel to impact a sample adhered to the impact end of the Kolsky bar with a low strength adhesive material, see Fig. 3(a). For front face impact, a sample adhered to a striker was fired from the gun barrel to impact on the Kolsky bar, see Fig. 3(b). The two impact tests result in different plastic shock wave propagation within a sample with the directions of the plastic shock wave propagation being opposite. As demonstrated in Electronic Supplementary material, Appendix A, the peak strengths of honeycomb specimens achieved in both back face impact and front face impact are nearly identical for lower velocity impact ($v_0 \leqslant 20\ \mathrm{ms}^{-1}$) and higher velocity impact ($v_0 \geqslant 80\ \mathrm{ms}^{-1}$). The Kolsky bar was positioned 110 mm from the open end of the gas gun, and had a diameter identical to that of the strikers, 27.5 mm, and a length of 1.8 m. Both the Kolsky bar and the strikers were made from M300 maraging steel with elastic modulus of 210 GPa and yield strength of 1900 MPa. The Kolsky bar was supported by four knife-edge friction-reducing Nylatron bearings and momentum was resisted at the distal end by an ACE MA 4757M self-adjusting shock absorber. Two diametrically opposite 120 Ω TML foil strain gauges of gauge length 1 mm in a half-Wheatstone bridge were located at the centre point. The stress history was recorded as a voltage change from the strain gauges, which was amplified by a Vishay 2310B signal conditioning amplifier system before being recorded on an Instek GDS-1052-U 50 MHz 2-channel Digital Oscilloscope. During signal capture, the two strain gauges on diametrically opposite sides allowed for a simple check of any bending in the Kolsky bar. Bending will produce sinusoidal oscillations with a π phase-difference between the two channels. If negligible bending was recorded during the testing, the results were accepted and the average value of the two gauges was taken.

Three cylindrical strikers of different masses were employed in the impact tests in order to achieve different striker velocities: a small striker of length $l = 0.02$ m and mass $M = 0.0927$ kg was used at velocity range of $80 \leqslant v_0 \leqslant 120\ \mathrm{ms}^{-1}$, an intermediate striker of length $l = 0.1$ m and mass $M = 0.463$ kg for velocity range $20 \leqslant v_0 \leqslant 80\ \mathrm{ms}^{-1}$, and a larger striker of length $l = 0.5m$ and mass $M = 2.3$ kg for lower velocity range $2.5 \leqslant v_0 \leqslant 20\ \mathrm{ms}^{-1}$. The effect of the striker mass on the compressive response of the honeycombs has been examined in Electronic Supplementary material, Appendix B. It is demonstrated that (i) the striker is subjected to significant deceleration during the lower velocity impact events, e.g. $v_0 \leqslant 20\ \mathrm{ms}^{-1}$, and the deceleration is negligible for the higher velocity impact events, e.g. $v_0 \geqslant 80\ \mathrm{ms}^{-1}$, and (ii) striker mass has a small effect on the compressive response under the higher velocity impact. The striker was accelerated using a pressurised gas gun of barrel length 3.5 m, internal diameter of 28 mm and outer diameter of 40 mm. Either compressed air (for lower velocity) or pressurised nitrogen (for higher velocity) was used to propel the striker to velocities in the range $2.5 \leqslant v_0 \leqslant 120\ \mathrm{ms}^{-1}$. Striker velocity was measured using two laser gates located at the open end of the gas gun barrel and confirmed with the high speed camera. High-speed photography was also employed to measure the response of the honeycomb specimens; the frame rate was typically 70,000 fps and the exposure time was 8 μs. As indicated in Section 5.2.1, the force equilibrium in honeycomb specimen was achieved wthin the time scale of the dynamic compression.

Calibration of the Kolsky pressure bar was conducted via direct impact of a striker (without a specimen) to trigger a stress wave within

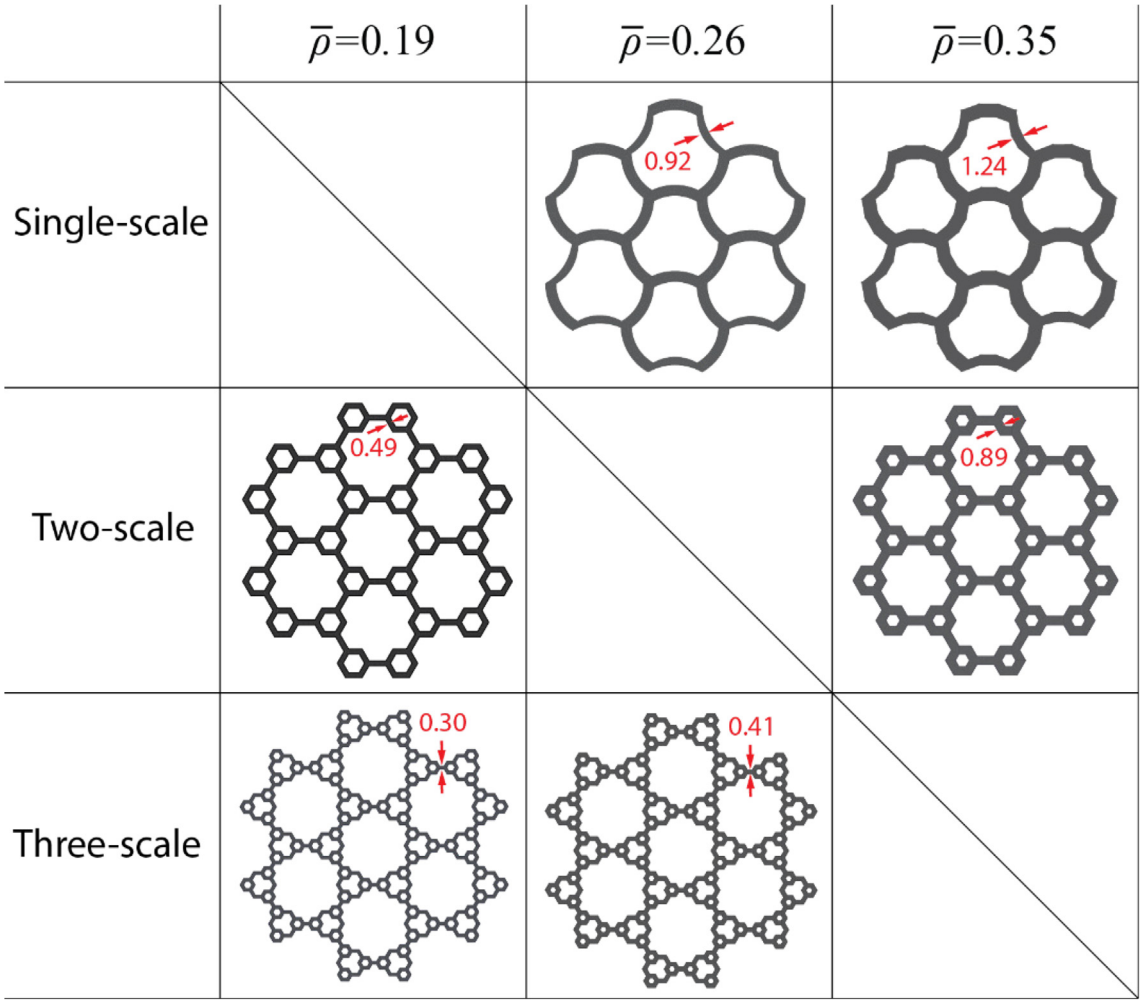

Fig. 6. The cross-sectional views of the single-scale, two-scale and three-scale honeycombs for finite element prediction. All dimensions are in mm.

the bar. Fig. 4 shows the measured time history of stress with a striker velocity of $v_0 = 4.1\ \mathrm{ms}^{-1}$. The measurement is compared with the predicted stress based on 1D elastic wave theory, which states that the axial stress within the bar can be calculated as $\sigma_E = \rho_s c v_0/2 = 77.1\ MPa$ with ρ_s and c as the bar density and longitudinal elastic wave speed, respectively. The average stress throughout the calibration test was measured as 78.5 MPa, within 2% of the prediction. The longitudinal elastic wave speed, c, was measured experimentally as the time taken for the reflection of the compressive wave from the distal end of the Kolsky bar returning to the strain gauges as a tensile wave. It was measured as $4865\ \mathrm{ms}^{-1}$, giving a time taken for reflection and thus complication of the stress measurement as 370 μs.

4. Finite element simulation

4.1. The finite element model

Numerical simulation was conducted to simulate both the quasi-static and dynamic compressive response of the honeycombs in order to (i) verify the experimental measurements, and (ii) develop further understanding of the effects of the key experimental parameters. The explicit version of the commercially available finite-element (FE) package ABAQUS® was employed in the FE calculations. The webs of the honeycomb specimens were modelled with 8-node linear 3D solid elements (ABAQUS element C3D8R). Numerical study confirmed that a maximum element edge length of half the wall thickness was required to achieve converged results. The FE model of a honeycomb was sandwiched between two rigid plates (discretised with the 4-node rigid elements, R3D4) in the 3-axis direction: one of the rigid plates was fully clamped, and the other rigid plate was restricted to translation in the 3-axis direction.

For quasi-static compression, the movable rigid plate imposed compressive loading on the sample with a constant velocity. To ensure the simulation was quasi-static, the velocity was controlled so that the kinetic energy was under 5% of the total energy in the system. In the dynamic simulation, the movable rigid plate was associated with a point mass and an initial velocity that were identical to those of the strikers employed in the experiment. For front face impact, the honeycombs were tied to the movable rigid plate and moved with the rigid plate to impact on the clamped rigid surface. For back face impact, the honeycombs were tied to the clamped rigid plate and crushed by the movable rigid plate. High-speed photographs of the experiments showed that negligible sliding occurred at the interfaces between the honeycomb, the striker and Kolsky bar. Hence, the tie constraint is appropriate. For all calculations, a penalty contact approach was employed to simulate the interaction between all the surfaces, with friction coefficient 0.5. This was sufficient as tests showed that the simulation results were not sensitive to the value of the friction coefficient employed in the calculations.

Numerical simulations were conducted to examine the effect of initial geometrical imperfections of the honeycombs, as shown in Electronic Supplementary material, Appendix C. It is suggested that the imperfections have a negligible effect on the compressive response of the honeycombs. An element deletion technique was employed to

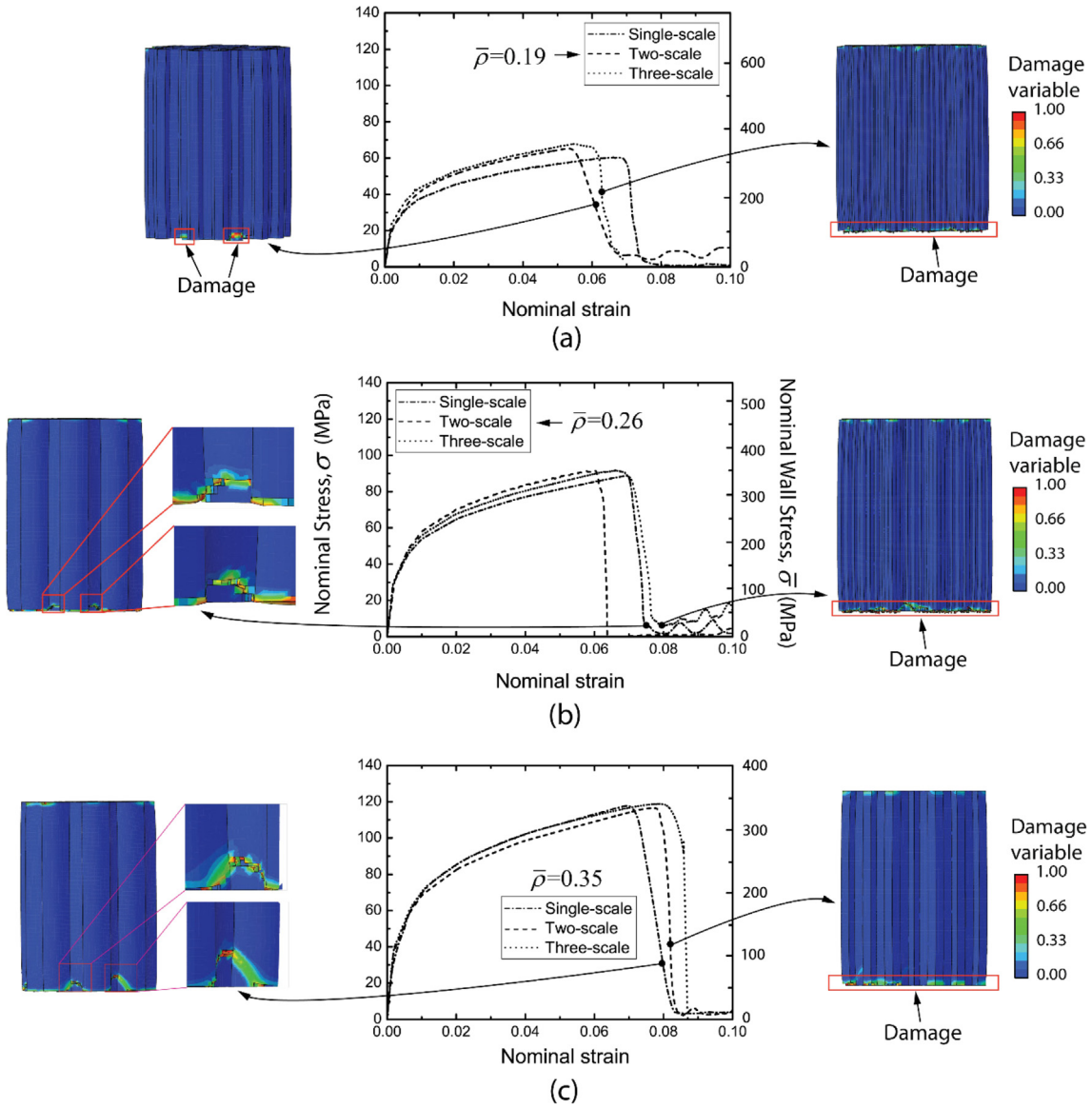

Fig. 7. Finite element predictions for honeycombs under quasi-static compression, including the compressive stress–strain relations and the damage mechanisms of the three types of honeycombs at relative density of (a) $\bar{\rho}$ = 0.19, (b) $\bar{\rho}$ = 0.26, (c) $\bar{\rho}$ = 0.35. The damage mechanisms of honeycombs which have been shown in Fig. 5 are not included in this figure.

remove elements from meshes when the damage variable d of the element reached the maximum value d = 1.0.

4.2. The constitutive model and material parameters

The constitutive model for the parent material of the honeycombs, AlSi10Mg alloy, should include elasticity, rate dependent plasticity, and damage. The elastic response was modelled using a linear elasticity model for an isotropic solid with Young's modulus E and Poisson's ratio ν. E and ν were measured via a uniaxial coupon tensile test, see Section 2.3. For the quasi-static simulation, the J2 yield criterion in conjunction with isotropic hardening was employed to model plasticity of the material. The experimental data obtained from coupon uniaxial tension along both 3-axis and 1-axis/2-axis (Fig. 2) were used as the inputs to the constitutive model to specify the yield stress–plastic strain relationship. However, the data from 1-axis/2-axis uniaxial tension gave the best agreement between numerical simulations and experimental measurements for the quasi-static compressive response of honeycombs, see Electronic Supplementary material, Appendix D. Numerical studies of the honeycombs under high strain-rate compression suggested that the development of plasticity in the parent material was strain rate dependent. The following model was used to capture the rate dependency in the simulations.

$$k = 1 + C\ln(\dot{\varepsilon}_p/\dot{\varepsilon}_o) \tag{1}$$

where C and $\dot{\varepsilon}_o$ are a material constant and the reference strain rate for quasi-static testing, respectively; $\dot{\varepsilon}_p$ is the von Mises equivalent plastic strain rate, and k is the enhancement factor, $k = \sigma_d/\sigma_o$, where σ_d is the yield stress at $\dot{\varepsilon}_p$ and σ_o the yield stress at $\dot{\varepsilon}_o$. In the simulations, the value of C was obtained via calibration against dynamic testing of the honeycombs, and $\dot{\varepsilon}_o$ was chosen to be the same as the strain rate used in quasi-static testing, i.e. $\dot{\varepsilon}_o = 10^{-3}\ s^{-1}$.

Damage initiation in the AlSi10Mg was assumed to occur when the von Mises equivalent plastic strain reached a critical value, ε_c. After initiation of damage, a damage variable, d ($0 \leqslant d \leqslant 1.0$), was assumed to develop based on the following relation

$$\dot{d} = \frac{L_e \sigma_s}{2G_f}\dot{\varepsilon}_p \tag{2}$$

where G_f is the fracture energy, L_e the characteristic element size and σ_s

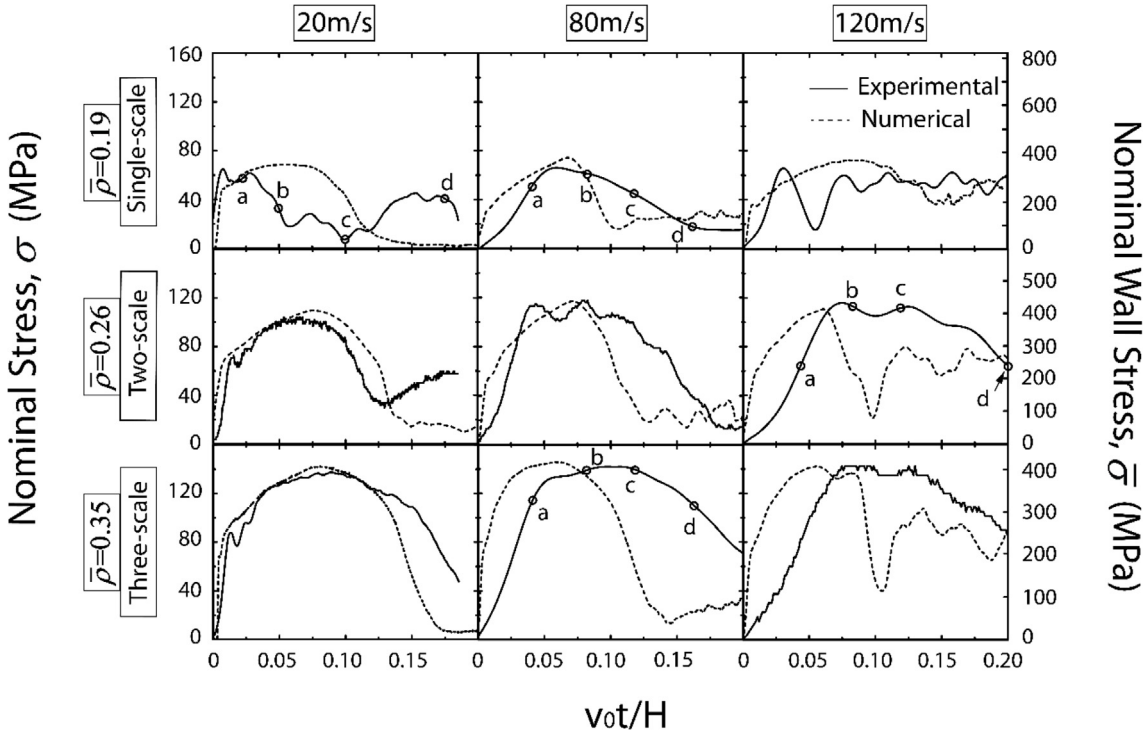

Fig. 8. Compressive stress as a function of normalised time $v_0 t/H$ obtained by the back face impact test at low (v_0 = 20 ms^{-1}), medium (v_0 = 80 ms^{-1}) and high velocities (v_0 = 120 ms^{-1}). The hollow circle "○"marks the stresses at the selected time instants in Fig. 9 – Fig. 12.

the yield stress at the initiation of damage. The fracture energy G_f is defined as

$$G_f = \int_{\varepsilon_c}^{\varepsilon_f} L_e \sigma_o d\varepsilon_p \tag{3}$$

where ε_p is the von Mises equivalent plastic strain and ε_f is the equivalent plastic strain when failure occurs [29]. The material parameters, ε_c and ε_f, were obtained from the 1-axis/2-axis uniaxial tension of SLM manufactured coupons, see Section 2.3. The damage variable was set to zero at the initiation of the damage, and reduced the yield stress of the material according to the relation $(1-d)\sigma_o$. When the value of d in an element reached the maximum value 1.0, the element was removed from the mesh. The material properties used for finite element simulations are shown in Table 1. Fig. 2 shows the predicted 1-axis/2-axis tensile stress–strain relations at strain rates ranging from 10^{-3} s^{-1} to 5000 s^{-1}. The strain rate effect enhances the strength and increases the ultimate elongation of the parent material.

5. Results and discussion

5.1. Quasi-static compression

5.1.1. Experimental measurement and numerical prediction

Fig. 5(a)–(c) show representative stress–strain relations for the three types of honeycomb under quasi-static compression. The experimentally observed and numerically simulated failure modes are shown in Fig. 5(d)–(f) at selected compressive strains post failure. The contours shown in the simulation results (Fig. 5(d)–(f)) represent values of the damage variable d.

The single-scale honeycomb had an average peak compressive strength σ_Y = 51 *MPa* at relative density $\bar{\rho}$ = 0.19, which corresponds to a peak nominal wall stress (compressive strength/relative density) $\bar{\sigma}_{max}$ = 268 MPa. Higher peak nominal wall stresses were achieved by the hierarchical honeycombs, $\bar{\sigma}_{max}$ = 358 MPa for the two-scale honeycomb with peak compressive strength σ_Y = 93*MPa* at relative density $\bar{\rho}$ = 0.26, and $\bar{\sigma}_{max}$ = 337 MPa for the three-scale honeycomb with peak strength σ_Y = 118 *MPa* at relative density $\bar{\rho}$ = 0.35. It is notable from this that both hierarchical honeycombs showed similar peak nominal wall stresses that were significantly higher than seen with the single-scale honeycomb.

The single-scale honeycomb failed by local plastic buckling of walls followed by damage close to the base. The finite element simulation successfully captured this failure mechanism. The peak compressive stress of the honeycomb was achieved at the onset of damage. Further development of damage within the honeycomb walls led to a significant decrease of the compressive stress (Fig. 5(a)). The two-scale honeycomb failed with damage close to the bottom support, see Fig. 5(e), and no wall buckling was observed throughout the experiment. The three-scale honeycomb specimen failed catastrophically through global plastic buckling, which may have been triggered by the damage of the parent material. Local plastic buckling was not observed in the experiment for either of the hierarchical honeycombs. This may be ascribed to the in-plane structures of the hierarchical honeycombs possessing higher structural stability.

The predicted compressive stress–strain relationships and failure mechanisms agree well with those obtained from the experiments for the single-scale and two-scale honeycombs. However, there is certain discrepancy in prediction of the global plastic buckling mode in comparison with the experimental measurements for the three-scale honeycomb, as shown in Fig. 5(f). This discrepancy may be attributed to the asymmetrical flaws induced by damage of the parent material, which was not accurately captured in the finite element simulations.

5.1.2. Effect of relative density on quasi-static compression

As mentioned in Section 2.1, the geometrical parameters of honeycomb samples were limited by the manufacturing resolution of the SLM manufacturing facility, and the three types of honeycombs have different relative densities. To evaluate the effect of relative density, the verified FE simulation is employed to examine the quasi-static compressive response of the three types of honeycombs with identical density. The cross-sectional views of each type of honeycomb are presented in Figs. 1 and 6. The predicted quasi-static compressive

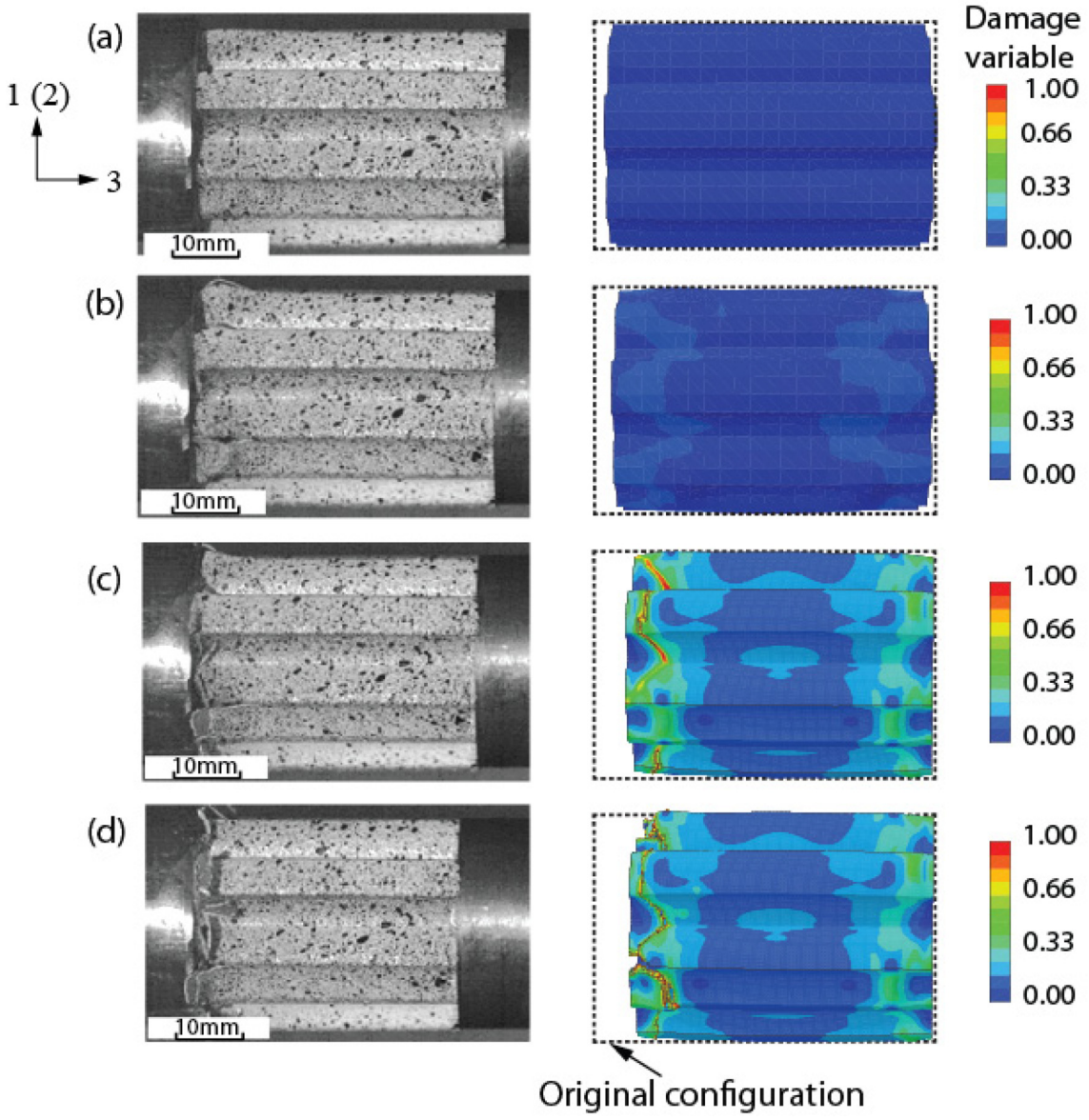

Fig. 9. Montage of the single-scale honeycomb under back face impact at the velocity of 20 ms^{-1} obtained from experiment and numerical simulations. Time t = 0 corresponds to the time instant when the steel striker impacted on the honeycomb. The images were taken at (a) t = 50 μs, (b) t = 100 μs, (c) t = 200 μs, (d) t = 350 μs, respectively.

stress–strain relations and the failure mechanisms of selected honeycombs are shown in Fig. 7. The failure mechanism of the single-scale honeycomb is sensitive to relative density, i.e. the failure mechanism changed from plastic buckling of walls at lower relative density ($\bar{\rho} = 0.19$) to the local damage of parent material without buckling at the bottom support at higher relative density ($\bar{\rho} \geqslant 0.26$). However, the failure mechanism of the two hierarchical honeycombs is not sensitive to relative density, i.e. parent material damage at the bottom support without buckling. This may be ascribed to the in-plane structures of the hierarchical honeycombs possessing higher structural stability. The nominal compressive strengths of both the two-scale and three-scale honeycombs are higher than that of the single-scale honeycomb at low relative density of $\bar{\rho} = 0.19$ owing to different failure mechanisms. For higher relative density ($\bar{\rho} \geqslant 0.26$), the nominal compressive strengths of the three types of honeycombs are nearly identical as all of the honeycombs failed with parent material damage at the bottom support.

5.2. Dynamic compressive response of the honeycombs

5.2.1. Back face impact

In this section, we first examine the dynamic response of the honeycombs shown in Fig. 1. Fig. 8 shows the nominal compressive stress of the honeycomb structures as a function of normalised time $v_0 t/H$ for three selected impact velocities in the back face impact test, with $t = 0$ corresponding to the beginning of the impact. As the Young's elastic modulus and density of the AlSi10Mg alloy parent material are measured as $E = 69.3$ GPa and $\rho_0 = 2670\ kg{\cdot}m^{-3}$, respectively, the longitudinal elastic wave speed propagated in the honeycombs can be calculated through $c_0 = \sqrt{\frac{E}{\rho_0}} = 5095\ ms^{-1}$. According to the experimental results shown in Fig. 8, the peak strengths of the honeycombs were achieved at $t \approx 24\,\mu s$ for impact velocity of $v_0 = 120\ ms^{-1}$. Hence, around three elastic-wave reflections took place in the honeycomb specimen of $H = 40$ mm before the peak strength of the honeycombs achieved. At lower impact velocities, i.e. $10 \leqslant v_0 \leqslant 80\ ms^{-1}$, there were more elastic-wave reflections because the time increased before

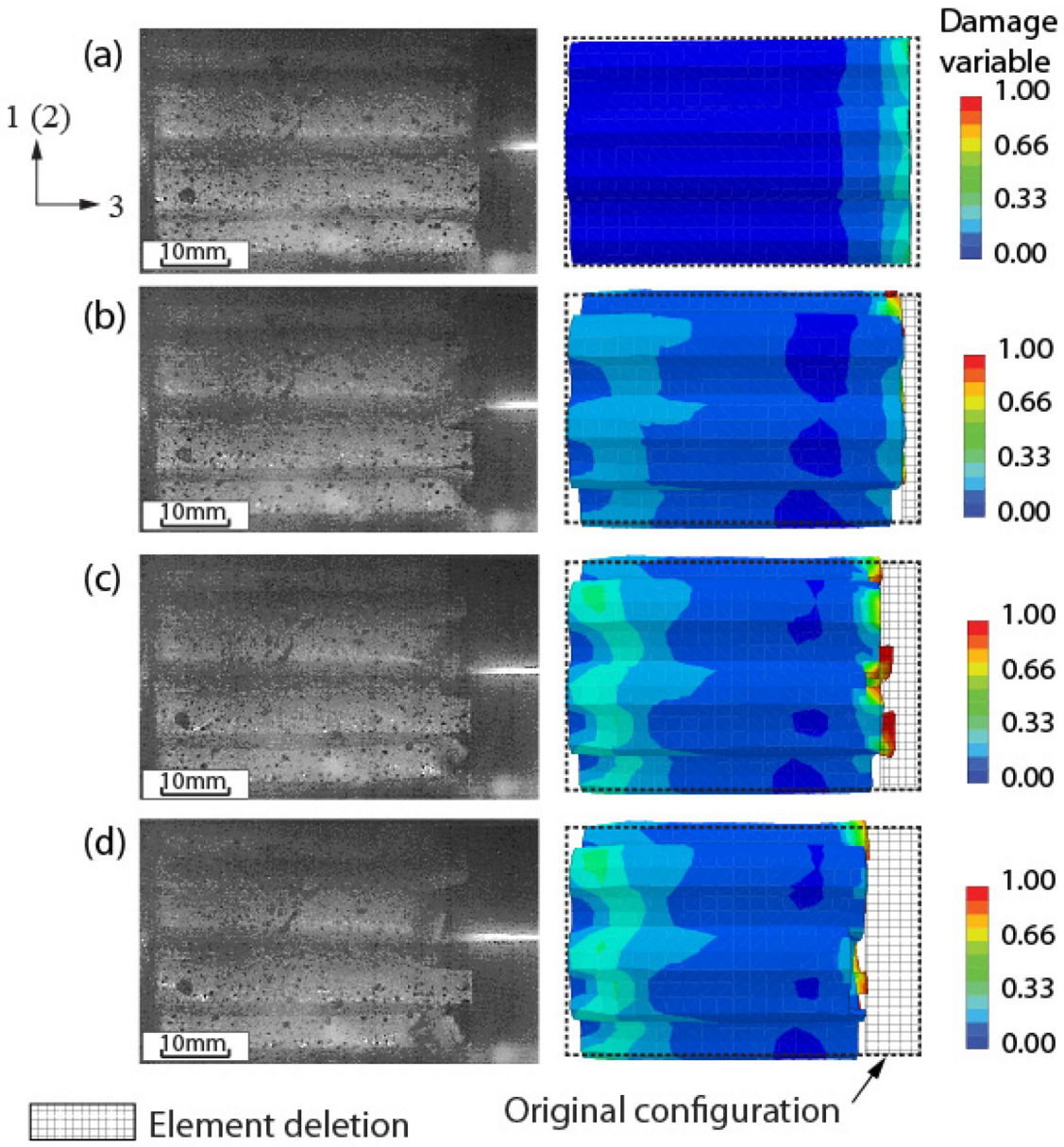

Fig. 10. Montage of the single-scale honeycomb under back face impact at the velocity of 80 ms^{-1} obtained from experiment and numerical simulations. Time t = 0 corresponds to the time instant when the steel striker impacted on the honeycomb. The images were taken at (a) t = 20 μs, (b) t = 40 μs, (c) t = 60 μs, (d) t = 80 μs, respectively.

achieving peak compressive stress of honeycombs. Thus, the force equilibrium has been achieved when measuring the peak compressive strength of honeycombs [30]. As shown in Electronic Supplementary material, Appendix A, the peak dynamic compressive strengths of honeycomb specimens are not sensitive to which of the two dynamic test methods investigated, i.e. the back face impact and the front face impact. Hence, only the results from the back face impact test are presented here. Both the finite element simulations and experimental measurements are shown in the figure for comparison. As shown in Electronic Supplementary material, Appendix B, numerical simulations demonstrated that the striker decelerated significantly during lower velocity impact events, e.g. 10–20% deceleration for $v_0 = 20\ ms^{-1}$, and the deceleration is negligible for higher velocity impact events, e.g. $v_0 \geqslant 80\ ms^{-1}$. Hence, the normalised time $v_0 t/H$ is equivalent to nominal compressive strain for the velocities $v_0 = 80\ ms^{-1}$ and $v_0 = 120\ ms^{-1}$ but not for the lower velocity $v_0 \leqslant 20\ ms^{-1}$. Compared with the quasi-static compressive response (Fig. 5(a)–(c)), dynamic compression enhanced the peak compressive strengths of the honeycombs. In contrast to catastrophic failure under quasi-static compression, the dynamic compressive stresses decreased steadily after the peak values were achieved. The agreement for peak strengths of honeycombs between finite element simulations and experimental measurements is reasonably good, however, the element deletion technique employed in the numerical simulations altered the mass matrix when elements were removed from the FE meshes, potentially making the simulation results more oscillatory than the experimental measurements for post-failure response. In addition, the geometrical flaws induced by additively manufactured process may increase the discrepancy between experimental measurements and FE simulations, as the flaws were not modelled in the FE simulations.

The failure modes of the honeycombs are revealed from montages of high-speed photographic images recorded at selected time instants (Points a, b, c and d in Fig. 8) during the impact events, as shown in Figs. 9 through 12. In these figures, the high-speed

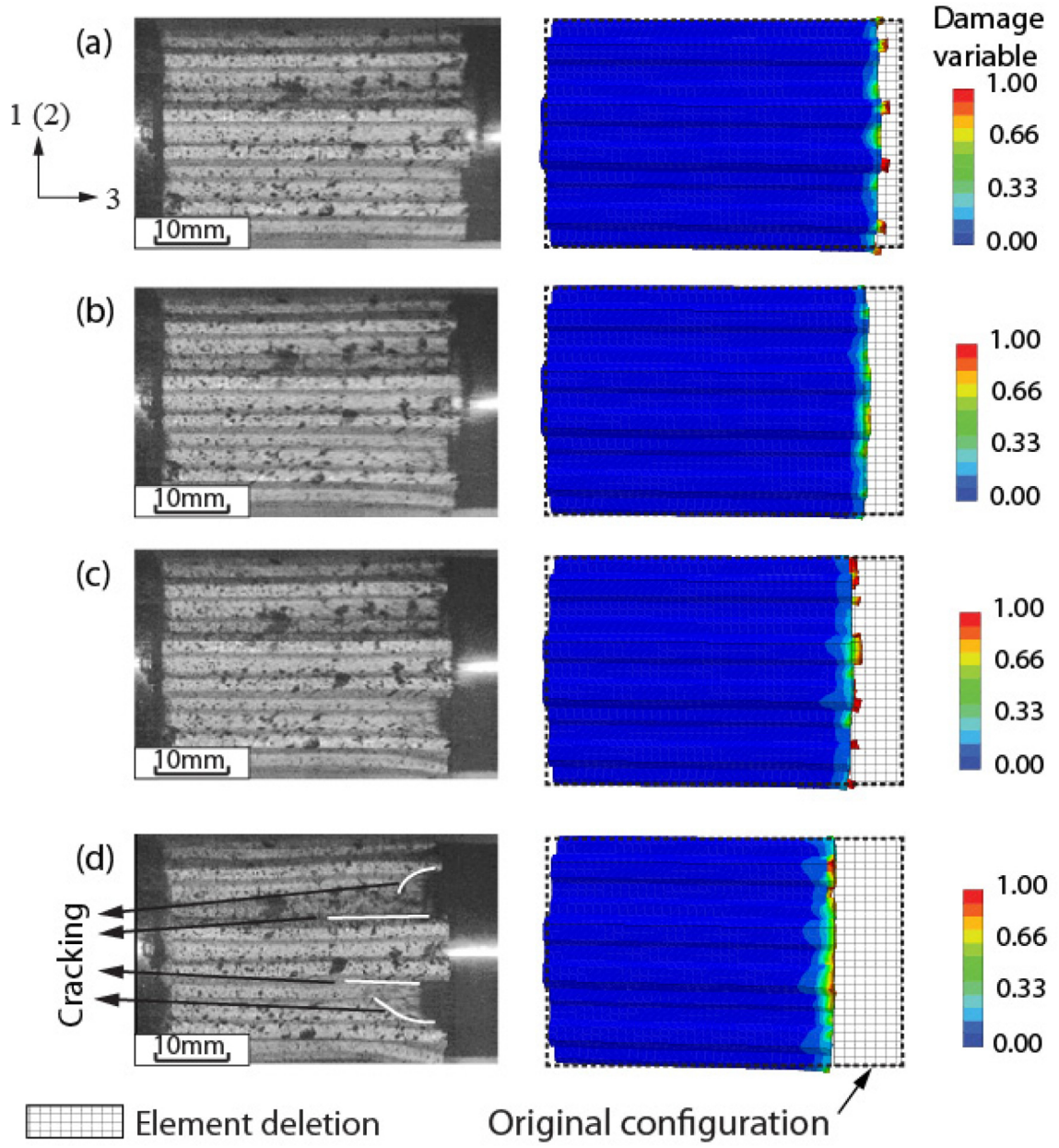

Fig. 11. Montage of the two-scale honeycomb under back face impact at the velocity of 120 ms^{-1} obtained from experiment and numerical simulations. Time t = 0 corresponds to the time instant when the steel striker impacted on the honeycomb. The images were taken at (a) t = 13.3 μs, (b) t = 26.7 μs, (c) t = 39.9 μs, (d) t = 66.5 μs, respectively.

photographic images are compared to FE predictions. Figs. 9 and 10 show montages of single-scale honeycombs under the impact of the striker with $v_0 = 20\ ms^{-1}$ and $v_0 = 80\ ms^{-1}$, respectively. The failure mechanism of the honeycomb under dynamic impact is similar to that under quasi-static compression, i.e. the honeycomb failed with plastic buckling of walls followed by damage close to the end attached to the Kolsky bar, at impact velocity of $v_0 = 20\ ms^{-1}$ (Fig. 9). However, at the velocity of $v_0 = 80\ ms^{-1}$ (Fig. 10), the plastic buckling damage in single-scale honeycomb was less significant owing to the micro inertial effects. Finite element simulations captured the failure mechanisms accurately, with element deletion activated when the peak stress was achieved ($d = 1$).

As the response under the lower velocity impact ($v_0 = 20\ ms^{-1}$) is essentially quasi-static, Figs. 11 and 12 only show the montages of the two-scale honeycomb and the three-scale honeycomb under higher speed impact ($v_0 \geqslant 80\ ms^{-1}$), respectively. For both hierarchical honeycombs, the montages taken from experiments suggest the damage started to develop at the impacted end. The specimens failed with significant plastic deformation and cracking. No wall buckling was observed throughout the experiments on hierarchical honeycombs. The FE simulation captured the failure mechanism for the two-scale honeycomb sample; the element deletion being activated at the impacted end. However, there is some discrepancy in prediction of the failure mechanism for the three-scale honeycomb sample; although the damage initially developed at the impacted end, the element deletion was first activated at the distal end of the sample.

To examine the effect of the relative density of the honeycomb structures, numerical simulations were conducted based on the geometries shown in Figs. 1 and 6. The outcomes are shown in Fig. 13 for peak wall stress $\bar{\sigma}_{max}$ normalised by the quasi-static 1(2)-direction tensile strength σ_T of the AlSi10Mg parent material as a function of v_0/H, and Fig. 14 for the nominal compressive stress as a function of

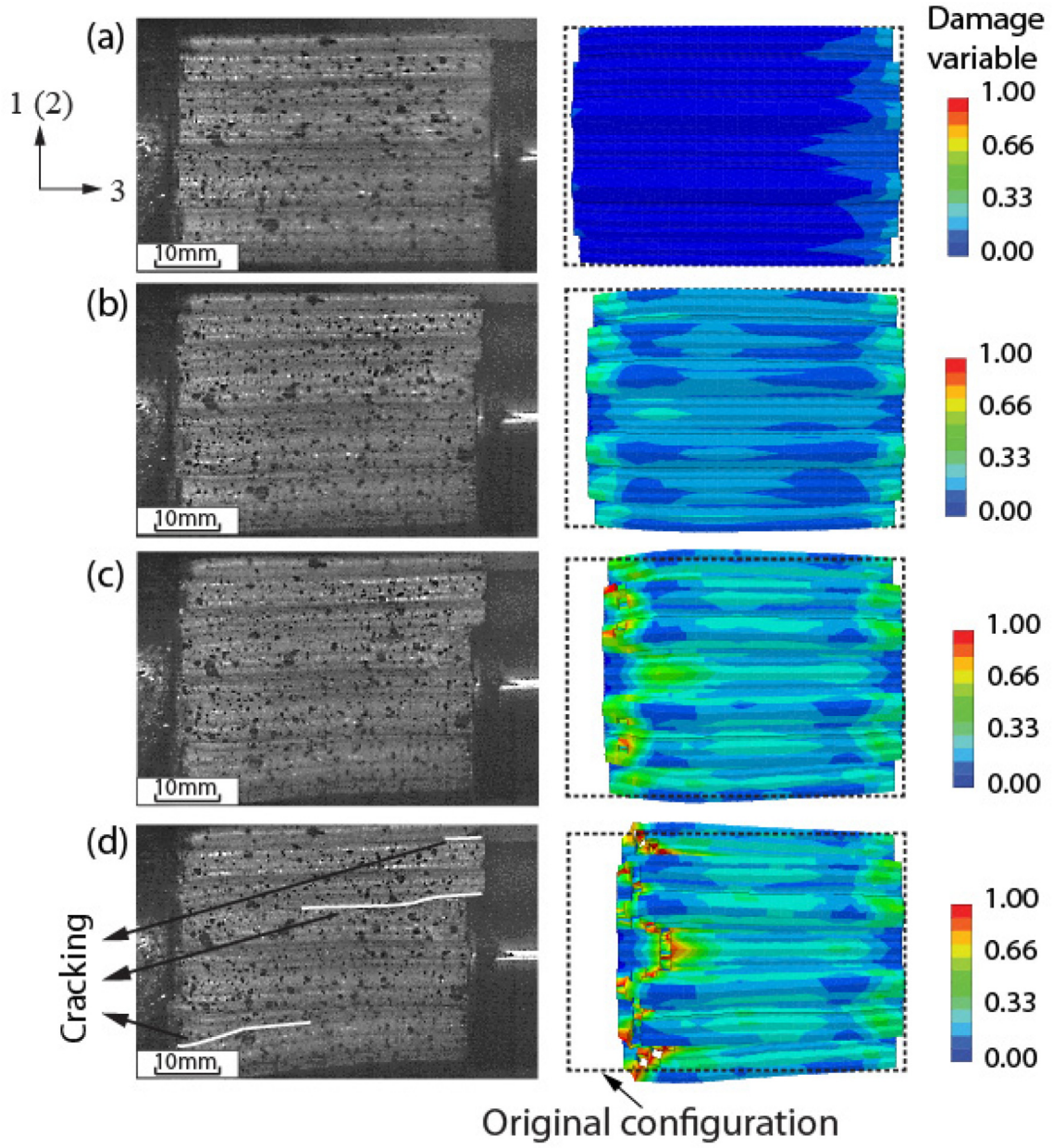

Fig. 12. Montage of the three-scale honeycomb under back face impact at the velocity of 80 ms^{-1} obtained from experiment and numerical simulations. Time t = 0 corresponds to the time instant when the steel striker impacted on the honeycomb. The images were taken at (a) t = 20 μs, (b) t = 40 μs, (c) t = 60 μs, (d) t = 80 μs, respectively.

normalised time $v_0 t/H$. The measured normalised peak wall stress for selected samples as well as the rate dependency of the parent material predicted using Eq. (1) are also included in Fig. 13 for comparison. The finite element predictions are in good agreement with the experimental measurements. The two hierarchical honeycombs have similar peak wall stresses throughout the densities considered as the failure mechanism is governed by damage of the parent material (Fig. 13). The measured and predicted trends of the strength enhancement of the two hierarchical honeycombs are similar to that predicted using the rate dependent material model (Eq. (1)), indicating that the strength enhancements at higher impact velocities may mainly be governed by the strain rate sensitivity of the parent material. At low relative densities, i.e. $\bar{\rho} = 0.19$, the single-scale honeycomb failed with wall plastic buckling as the peak wall stresses were significantly less than those of the two hierarchical honeycombs. With increase of relative density, say $\bar{\rho} \geqslant 0.26$, the failure mechanism of single-scale honeycomb is governed by damage of the parent material without wall plastic buckling. Hence, the difference in the peak wall stress is diminished, i.e. the three types of honeycombs have similar peak wall stresses when $\bar{\rho} \geqslant 0.26$. The time history of the dynamic response shown in Fig. 14 indicates that the two hierarchical honeycombs can absorb more energy than the single-scale honeycomb with identical relative density.

5.2.2. *Effect of strain rate sensitivity of the parent material*

As mentioned in Section 5.2.1, the strain rate dependency of the parent material is a key factor for dynamic strength enhancement of the honeycombs. To further understand this, Fig. 15 presents the predicted compressive responses of selected honeycombs with and without the parent material strain rate dependency for both back face and front face impact at low velocity impact (v_0 = 20 ms^{-1}) and high velocity impact (v_0 = 80 ms^{-1}). For low velocity impact (v_0 = 20 ms^{-1}), the dynamic response is similar to quasi-static compression, see analysis presented in

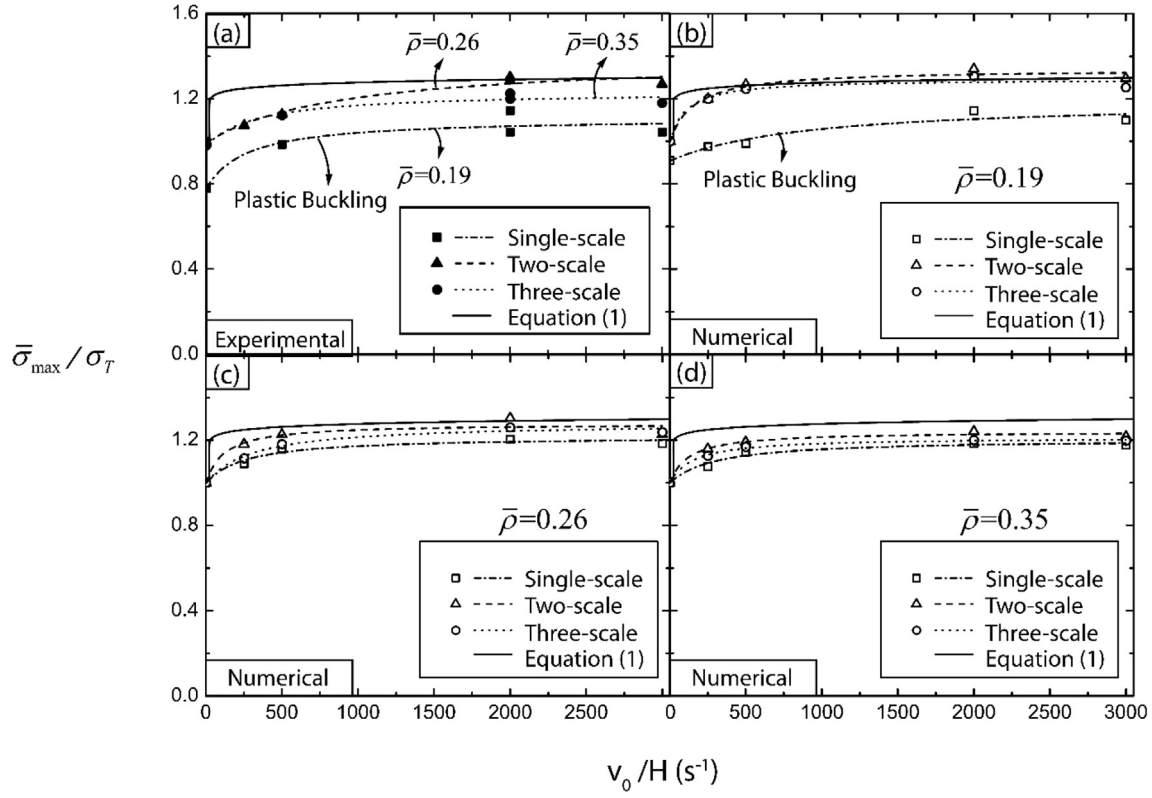

Fig. 13. The peak nominal wall stresses $\bar{\sigma}_{max}$ of the honeycombs normalised by the quasi-static 1(2)-axis tensile strength σ_T of the AlSi10Mg alloy parent material as a function of v_0/H. The experimental measurements (a) and numerical predictions of the honeycombs at the relative density of (b) $\bar{\rho}$ = 0.19, (c) $\bar{\rho}$ = 0.26, (d) $\bar{\rho}$ = 0.35 are presented.

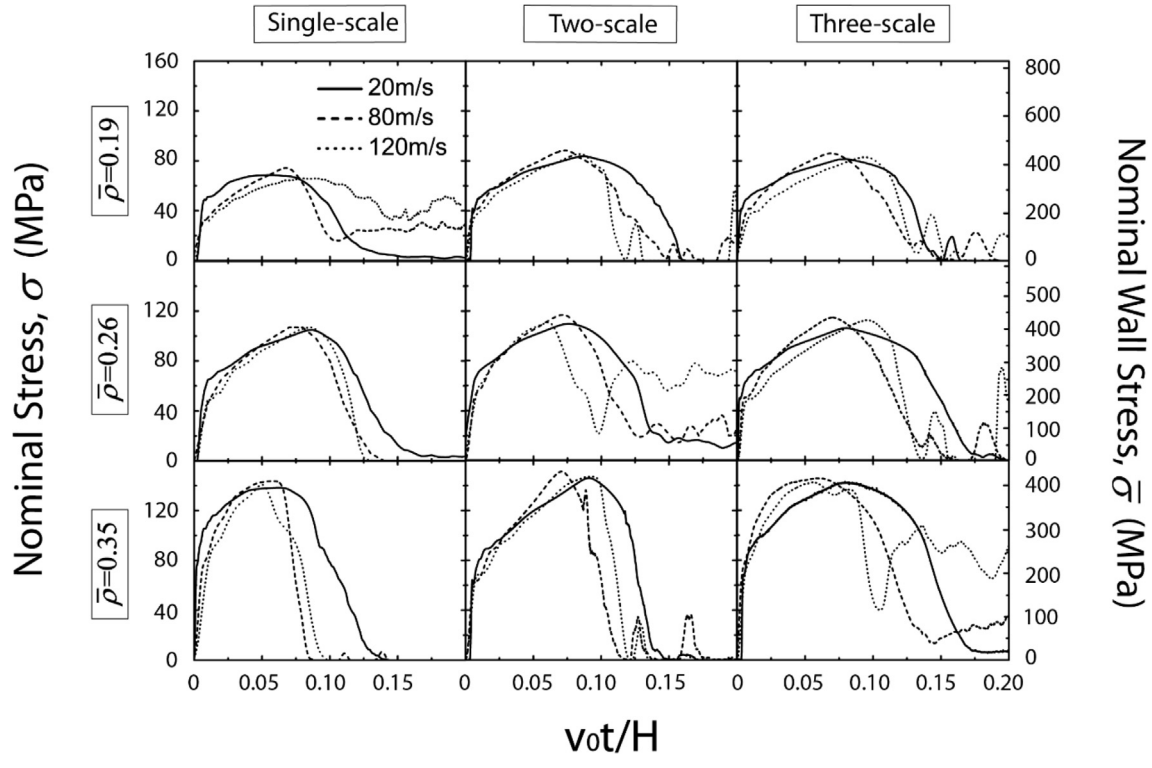

Fig. 14. Finite element predicted dynamic compressive responses of the three types of honeycombs at three different relative densities.

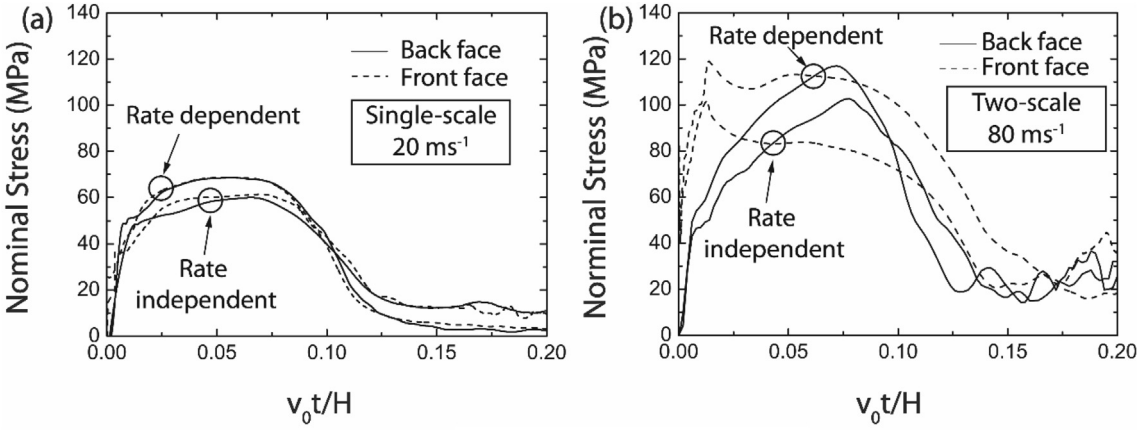

Fig. 15. Numerical study on the effect of strain rate sensitivity of the parent material. (a) The single-scale honeycomb impacted at the velocity 20 ms^{-1} and (b) the two-scale honeycomb impacted at the velocity 80 ms^{-1}.

Section 5.2.1. Hence, the effect of the parent material strain rate dependency is not significant. However, for high velocity impact (v_0 = 80 ms^{-1}), the effect becomes significant.

6. Concluding remarks

The out-of-plane quasi-static and high strain rate dynamic compressive responses of Selective Laser Melting (SLM) manufactured hierarchical honeycombs have been reported. Three types of honeycombs, i.e. single-scale, two-scale and three-scale, were manufactured from AlSi10Mg alloy. A Kolsky pressure bar was employed for the dynamic test with a striker velocity up to v_0 = 120 ms^{-1}. Validated finite element (FE) simulations were conducted to facilitate interpretation of the experimental measurements. Different failure mechanisms among these honeycombs have been identified for quasi-static and dynamic compression, i.e. transition of the plastic buckling of walls to the local damage of the parent material without buckling for the single-scale honeycomb when the relative density of the honeycomb increased, and damage of the parent material without buckling for both the two-scale and three-scale honeycombs at different relative densities of the honeycombs. The strength enhancement of the hierarchical honeycombs under dynamic compression is dominated by the strain rate sensitivity of the parent material. The micro-inertial effects under higher velocity impact ($v_0/H \geqslant 500s^{-1}$) also enhance the dynamic compressive strength of the single-scale honeycomb. The two-scale and three-scale hierarchical honeycombs can offer higher peak nominal wall stresses compared to the single-scale honeycomb at the low relative density ($\bar{\rho}$ = 0.19); The difference is diminished as relative density increases, i.e. the three types of honeycombs can achieve similar peak wall stresses when $\bar{\rho} \geqslant 0.26$. Numerical results have suggested the hierarchical honeycombs can offer better energy absorption capacity than the single-scale honeycomb. The two-scale and three-scale hierarchical honeycombs have achieved similar peak nominal wall stresses for both quasi-static and dynamic compression, which may suggest that the structural performance under out-of-plane compression is not sensitive to the hierarchical architecture. The structural advantage of the hierarchical honeycombs can be utilised to develop high performance metallic lightweight structural components.

In order to capture the constitutive response of the SLM AlSi10Mg alloy, a uniaxial tension coupon test was conducted, which has shown that the parent material had anisotropic plasticity and damage. The constitutive model for the parent material employed in the simulations included elasticity, rate dependent plasticity and damage. However, the anisotropic plasticity and damage of the parent material were not included. FE simulations were seen, in general, to be in good agreement with experimental measurements. The failure modes of the honeycombs have been captured reasonably by FE predictions.

Acknowledgements

This work was supported by the Engineering and Physical Sciences Research Council, UK [grant number EP/I033335/1]. The authors also acknowledge the use of High Performance Computing facility provided by the University of Nottingham for finite-element numerical simulation. YZ would like to acknowledge the financial support of China Scholarship Council (CSC).

Supplementary data

Supplementary data associated with this article can be found, in the online version, at http://dx.doi.org/10.1016/j.compstruct.2018.04.021.

References

[1] Gibson LJ, Ashby MF. Cellular solids: structure and properties. Cambridge, UK: Cambridge University Press; 1997.
[2] Wicks N, Hutchinson JW. Optimal truss plates. Int J Solids Struct 2001;2000(38):5165–83.
[3] Liu T, Deng ZC, Lu TJ. Bi-functional optimization of actively cooled, pressurized hollow sandwich cylinders with prismatic cores. J Mech Phys Solids 2007;55(12):2565–602.
[4] Fleck NA, Deshpande VS, Ashby MF. Micro-architectured materials: past, present and future. Proc R Soc London, Ser A 2010;466(2121):2495–516.
[5] Fan HL, Jin FN, Fang DN. Mechanical properties of hierarchical cellular materials. Part I: analysis. Compos Sci Technol 2008;68(15–16):3380–7.
[6] Deshpande VS, Ashby MF, Fleck NA. Foam topology bending versus strain stretching dominated architectures. Acta Mater 2001;49:1035–40.
[7] Haghpanah B, et al. Self-similar hierarchical honeycombs. Proc R Soc London, Ser A 2013;469(2156). 20130022-20130022.
[8] Ajdari A, et al. Hierarchical honeycombs with tailorable properties. Int J Solids Struct 2012;49(11–12):1413–9.
[9] Oftadeh R, et al. Optimal fractal-like hierarchical honeycombs. Phys Rev Lett 2014;113(10):104301.
[10] Lakes R. Materials with structural hierarchy. Nature 1993;361(6412):511–5.
[11] Khan MK, Baig T, Mirza S. Experimental investigation of in-plane and out-of-plane crushing of aluminum honeycomb. Mater Sci Eng, A 2012;539:135–42.
[12] Radford DD, et al. Dynamic compressive response of stainless-steel square honeycombs. J Appl Mech 2007;74(4):658.
[13] Xue Z, Hutchinson JW. Crush dynamics of square honeycomb sandwich cores. Int J Numer Meth Eng 2006;65(13):2221–45.
[14] Tao Y, et al. Strain rate effect on the out-of-plane dynamic compressive behavior of metallic honeycombs: experiment and theory. Compos Struct 2015;132:644–51.
[15] Xu S, et al. Experimental study of the out-of-plane dynamic compression of hexagonal honeycombs. Compos Struct 2012;94(8):2326–36.
[16] Zhang Y, et al. Out-of-plane crashworthiness of bio-inspired self-similar regular hierarchical honeycombs. Compos Struct 2016;144:1–13.
[17] Zhang B, et al. Magnetic properties of in-situ synthesized FeNi3 by selective laser melting Fe-80%Ni powders. J Magn Magn Mater 2013;336:49–54.
[18] Kempen K, et al. Mechanical properties of AlSi10Mg produced by selective laser melting. Physics Procedia 2012;39:439–46.

[19] Bauer J, et al. High-strength cellular ceramic composites with 3D microarchitecture. Proc Natl Acad Sci USA 2014;111(7):2453–8.
[20] Aboulkhair NT, et al. Improving the fatigue behaviour of a selectively laser melted aluminium alloy: influence of heat treatment and surface quality. Mater Des 2016;104:174–82.
[21] Aboulkhair NT, et al. Reducing porosity in AlSi10Mg parts processed by selective laser melting. Addit Manuf 2014;1–4:77–86.
[22] ASTM, E8/E8M-13a Standard Test Method for Tension Testing of Metallic Materials. 2013, Book of standard volume 0301: West Conshohocken: Amercian Society for Testing and Materials ASTM.
[23] Maskery I, et al. Quantification and characterisation of porosity in selectively laser melted Al–Si10–Mg using X-ray computed tomography. Mater Charact 2016;111:193–204.
[24] Aboulkhair NT, et al. The microstructure and mechanical properties of selectively laser melted AlSi10Mg: the effect of a conventional T6-like heat treatment. Mater Sci Eng, A 2016;667:139–46.
[25] Manfredi D, et al. From powders to dense metal parts: characterization of a commercial AlSiMg alloy processed through direct metal laser sintering. Materials 2013;6(3):856–69.
[26] Joseph S, Kumar S. A systematic investigation of fracture mechanisms in Al–Si based eutectic alloy—effect of Si modification. Mater Sci Eng, A 2013;588:111–24.
[27] Kolsky H. An Investigation of the mechanical properties of materials at very high rates of loading. Proc Phys Soc London, Sect B 1949;62:676–700.
[28] Liu T, Turner P. Dynamic compressive response of wrapped carbon fibre composite corrugated cores. Compos Struct 2016.
[29] ABAQUS, ABAUQS analysis user's manual, Version 6.14, ABAQUS, Inc. 2014.
[30] Russell Benjamin P, et al. Dynamic compressive response of composite corrugated cores. J Mech Mater Struct 2010;5:477–93.